Guided mode resonator coupled with nanocrystal intraband absorption

Adrien Khalili, Mateusz Weis, Simon Gwénaël Mizrahi, Audrey Chu, Tung Huu Dang, Claire Abadie, Charlie Gréboval, Corentin Dabard, Yoann Prado, Xiang Zhen Xu, et al.

Guided mode resonator coupled with nanocrystal intraband absorption

Adrien Khalili[1], Mateusz Weis[2], Simon Gwénaël Mizrahi [2], Audrey Chu[1], Tung Huu Dang[1], Claire Abadie[4], Charlie Gréboval[1], Corentin Dabard[4], Yoann Prado[1], Xiang Zhen Xu[4], Emmanuel Péronne[2], Clément Livache[5], Sandrine Ithurria[4], Gilles Patriarche[6], Julien Ramade[7], Grégory Vincent[3], Davide Boschetto[2], Emmanuel Lhuillier[1*]

[1] Sorbonne Université, CNRS, Institut des NanoSciences de Paris, INSP, F-75005 Paris, France.
[2] LOA, Laboratoire d'Optique Appliquée, CNRS, Ecole Polytechnique, ENSTA Paris, Institut Polytechnique de Paris, 181 Chemin de la Hunière et des Joncherettes, 91120 Palaiseau, France.
[3] ONERA - The French Aerospace Lab, 6, chemin de la Vauve aux Granges, BP 80100, F-91123 Palaiseau, France.
[4] Laboratoire de Physique et d'Etude des Matériaux, ESPCI-Paris, PSL Research University, Sorbonne Université Univ Paris 06, CNRS UMR 8213, 10 rue Vauquelin 75005 Paris, France.
[5]Chemistry Division, Los Alamos National Laboratory, Los Alamos, New Mexico 87545, United States
[6] Centre de Nanosciences et de Nanotechnologies, CNRS, Université Paris-Saclay, C2N, Palaiseau 2110, France.
[7]Institut Pprime, Département Physique et Mécanique des Matériaux, UPR 3346 CNRS, Université de Poitiers, SP2MI, TSA 41123, 86073 Poitiers Cedex 9, France

Abstract: Intraband absorption in doped nanocrystals offers an interesting alternative to narrow band gap materials to explore mid infrared optoelectronic device designs. However, the performance of such device clearly lags behind the ones relying on intrinsic materials. Livache *et al.* have proposed a dye sensitized approach to overcome the limitations observed from intraband materials (high dark current, slow response, low activation energy), where the intraband absorber is coupled to an undoped material which takes care of the charge conduction. Here, we unveil the coupling between both materials using mid-infrared transient reflectivity (TR) measurement. We show that hybrid material displays a unique feature in the TR signal that we attribute to a charge transfer and for which the dynamic matches the hopping time. We then developed a strategy to enhance the photodetection performances of the hybrid material by coupling for the first time intraband absorption to a light resonator. The latter is used to enhance the absorption by a factor 4 and enables an increase of the operating temperature by 80 K compared to the reference device. The obtained device matches the performance of best devices relying on intraband absorption.

Keywords: intraband absorption, mid-infrared, doped nanocrystals, mercury chalcogenides, optical resonator

*To whom correspondence should be sent: el@insp.upmc.fr

Intersub-band transitions have certainly been the highest realization of quantum-well-based technologies leading to devices such as quantum cascade lasers[1] and quantum-well infrared photodetectors.[2] Intraband transitions are their 0D equivalent occurring in quantum dots and nanocrystals (NCs). This transition is not limited by the bulk band gap, and they are inherently narrow energy transitions, well-suited to address the infrared range.

While the concept of intraband photoconduction has been demonstrated for NCs array of mercury[3–6], lead[7] and silver[8,9] chalcogenides, the level of performance achieved lags, by orders of magnitude, behind the one of quasi-intrinsic interband materials, at the same wavelength. In particular, low operating temperature, 80 K typically, remains necessary while HOT (high operating temperature) operation is achieved for interband materials.[10]

For pristine intraband NCs arrays, similar to intersub-band heterostructures, doping is mandatory to reach the targeted absorption. However, it comes at a high cost. Doping is responsible for a large dark current, making the photoconductive signal only a small fraction of the dark current, up to the point where, generally, bolometric slow response[11] prevails above the photoconductive signal. Recently, Livache *et al.*[12] demonstrated that the large dark current and slow time response can be tackled by replacing the pristine intraband NC array by a mixture of doped and undoped NCs. Specifically, doped HgSe NCs exhibiting intraband absorption are mixed with undoped HgTe NCs. The amount of HgTe in the mixture is chosen high enough to prevent percolation (*i.e.,* formation of a continuous transport path up to the electrode) of the electrons within the HgSe NC array. In this configuration, the mixture behaves as a mid-IR dye-sensitized solar cell, where HgSe absorbs the mid-IR light, while the HgTe particles drive the transport properties. While the concept is already established, the coupling between the two materials, particularly its dynamics remains unexplored. Here, using infrared transient reflectivity with a resolution of 50 fs, we provide evidence of charge transfer between the two materials.

Furthermore, although the mixture approach appears beneficial for dark current and time response, it also reduces the film absorbance compared to the pristine material, through a reduction of the intraband material volume fraction. Here, we show that by coupling the HgSe/HgTe metamaterial to a guided-mode resonator[13] (GMR) we can enhance the intraband absorption and its associated photocurrent. This resonator enables to maintain the photocurrent to dark current modulation while increasing the operating temperature by 80 K with respect to the metamaterial without the optical nano-resonator.

Intraband transitions in nanocrystals are an interesting alternative to interband transitions to achieve absorption of low energy, infrared photons. Moreover, it may pave the way toward new device possibilities similarly to what has been demonstrated based on quantum cascade devices in III-V semiconductor heterostructures.[1,14] The intraband absorption in the steady state requires doped nanoparticles.[15] However, a moderate level of doping (1 carrier per nanocrystal typically) is necessary to avoid plasmonic absorption in their inherent extremely short (<100 fs) photocarrier lifetime.[16] Among the few potential material[7–9] candidates we choose to focus on HgSe[3–5] since its electronic spectrum in the mid-IR has already been investigated, easing the further device integration.[17]

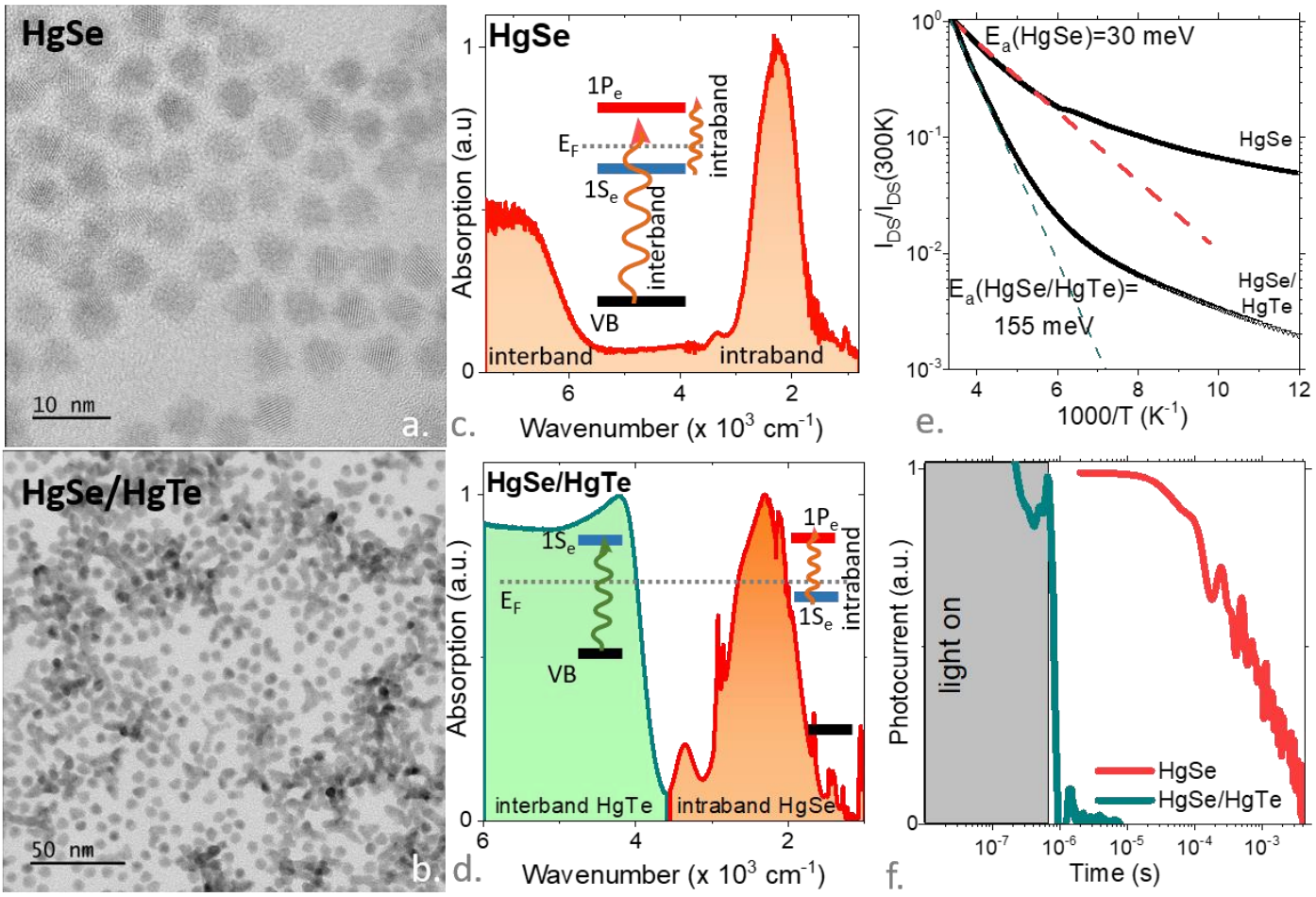

Figure 1 Intraband absorbing material properties*. a. TEM image of HgSe NCs. b. TEM image of HgSe/HgTe NC mixture. c. Absorption spectrum of HgSe NCs. The inset indicated the involved transistions. d. Absorption spectrum of the HgSe/HgTe NC mixture under an ink form. The inset indicated the involved transistions e. Normalized dark current value as a function of temperature for a film of HgSe NCs and for a film of a mixture of HgSe/HgTe NCs. The current is normalized by its value at 300 K. Dashed lines correspond to Arrhenius fits. f. Time response to a pulse (λ=4.4 µm) of light for a film of HgSe NCs and for a film of HgSe/HgTe NC mixture.*

We synthetize HgSe nanocrystals using the procedure developed by Lhuillier *et al*.[5] Briefly, mercury oleate reacts with trioctylphosphine selenium in oleylamine at a moderate temperature (100 °C). The obtained particles are quasi-round according to transmission electron microscopy (TEM) image (**Figure 1**a) with a mean size of 5 nm. The absorption spectrum includes two components (**Figure 1**c). At high energies (above 6000 cm^{-1}), there is a broadband interband absorption signal. At lower energies, there is no absorption until the intraband contribution around 2200 cm^{-1}. Here, we choose the particle size to match the HgSe intraband absorption and the 3 – 5 µm transparency window commonly described as mid-wave infrared (MWIR). As already stated in the introduction, although photoconductive, an array of HgSe NCs presents a weak transport activation energy (30 meV, see **Figure 1**e), leading to a lack of detection performance improvement upon cooling. Furthermore, the slow response (several ms, see **Figure 1**f) is not compatible with imaging applications. However, as it has been demonstrated by Livache *et al.*[12], both challenges can be solved by replacing the pristine HgSe array by a mixture of HgTe (Figure S1) and HgSe NCs. From TEM (**Figure 1**b, S2-4), the two types of particles can easily be distinguished since HgSe presents a quasi-spheric shape while HgTe is a tripod[18]. The absorption spectrum of the mixture preserves the intraband absorption of HgSe, while the contribution of HgTe now appears in the range of energy corresponding to the absorption gap (*i.e.,* 4000 cm^{-1}) between interband and intraband for HgSe, see **Figure 1**d. The

HgTe particle size is chosen such that the $1S_e$ state from HgTe is almost resonant with HgSe $1P_e$ state, see energy diagram revealed by X-ray photoemission in Figure S7. This is critical to ensure efficient charge transfer between the NCs. Empirically, the ratio of the two materials is determined in order that the relative magnitude of the intraband absorption of HgSe and the interband signal from HgTe is close to 1. In this case, the amount of HgTe is sufficient to prevent the transport percolation within the HgSe NCs array and the detection properties are improved. From **Figure 1**e, we observe a drastic increase of the transport activation energy, reaching now 155 meV, revealing that the dark current is strongly reduced under cryogenic condition. Additionally, the time response is strongly reduced and is as short as 1 µs, see **Figure 1**f.

Although the absorption of the mixture is set to achieve a similar optical density for both materials, the photocurrent spectrum reveals fairly different photocurrent contributions, see **Figure 2**. Measurements being conducted at 300 K for absorption and 80 K for photoconduction, the difference might result from a temperature effect. In Figure S6, we then conduct a systematic investigation of the pristine materials (HgSe and HgTe) and mixture absorption as a function of temperature. As the temperature is reduced, HgTe and HgSe interband gaps are reduced (*i.e.* redshift, +240 µeV.K^{-1} for HgTe), while the intraband gap of HgSe is increased (*i.e.* blueshift, -115 µeV.K^{-1}).[19,20] In the mixture, the same shifts are observed. On the other hand, the relative magnitude of the two absorption peaks is only marginally affected, see figure S6. Thus, the change of relative peak magnitude in the photocurrent rather relates to a transport process.

As a photon, which energy matches the intraband transition, is absorbed, an electron from the conduction band ground state ($1S_e$) is promoted to the excited state ($1P_e$) in a HgSe NC. This electron needs then to be transferred to the HgTe conduction band to contribute to transport and to the device's photocurrent. This charge transfer process makes that absorption and photocurrent spectra cannot be matched. The intraband contribution from HgSe to the photocurrent being only 1/6 of the one from the interband of HgTe, one can attribute the value of ≈17% to the whole charge transfer and transport process

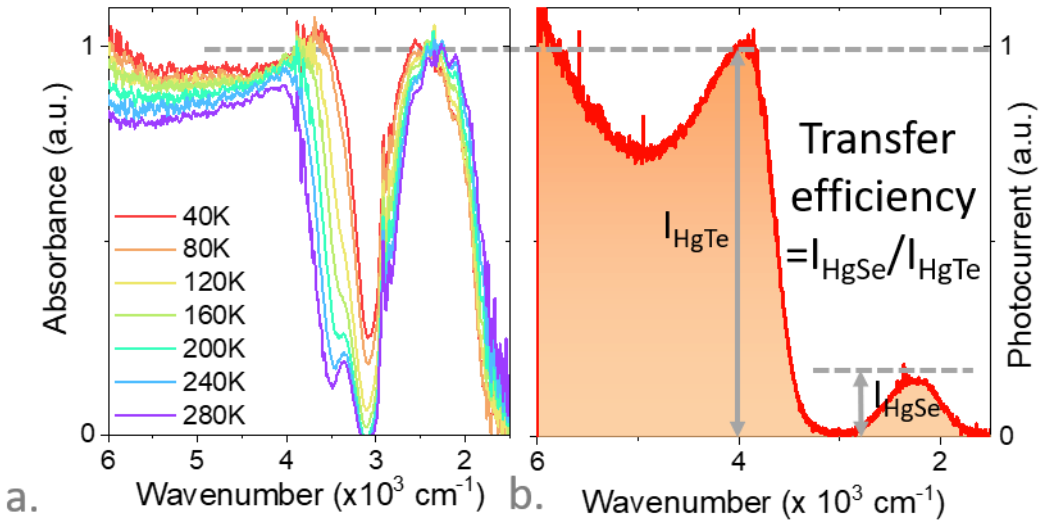

Figure 2 Charge transfer in HgSe/HgTe mixture*. Absorption at various temperatures (a.) and photocurrent at 80 K (b.) spectra of HgSe/HgTe NC mixture.*

This raises the need for a deeper analysis of the coupling between both populations, and particularly the dynamics of this transfer needs to be unveiled. To do so, we use IR transient reflectivity measurement in a pump-probe configuration. The setup is operated in a non-degenerate mode

where the pump operates at 800 nm (1.55 eV - 35 fs pulse duration) while the probe is set at 4 µm (0.32 eV - 50 fs pulse duration) matching the intraband gap of HgSe.

While this configuration does not exactly allow for accurate determination of exciton lifetimes and intrinsic processes in each of the host NCs, we propose a comparative analysis on transient signals measured for HgTe only, HgSe only and a HgSe/HgTe mixture. All samples are processed the same way as way as for photoconduction experiments (*i.e.,* with the same ligand exchange). Figure 3a shows the transient reflectivity signals for the three samples. The electronic structure of HgSe is schematized in **Figure 3**b. At rest, the Fermi level lies in the conduction band between the $1S_e$ and $1P_e$ states. Thus, valance band states are filled with electron while $1P_e$ state and upper states (called HS for hot states in **Figure 3**b) remain empty. With initial long ligand (DDT) the $1S_e$ state is mostly filled (2 electrons per NC), however after ligand exchange, the population of the NC appears to be slightly reduced (in the 0.2 to 2 electron per HgSe NC range, (see Figure S5).[11,17]

Under excitation, the pump is absorbed and a hot electron is generated. Note that due to the high energy of the pump with respect to the interband band gap, the initial electrons can either be located in the $1S_e$ state either in the valence band. In the latter case the carriers being less hot, they will thermalize on a shorter time scale since the cooling rate seems to be unaffected by the pump excitation in such NCs.[21] We observe a photon induced absorption (PIA with positive ΔR/R observed in regime I, lasting from 0 to 3 ps). A possible mechanism is that the hot charges generate a Stark effect that slightly affects the energy of the intraband transition, but other effects may be responsible to this early signal such as hot intraband transitions or a shift resulting from exciton-exciton interactions. As the electrons cool down (regime I), they will reach the $1P_e$ state, at which point the transient reflectivity signal will become negative due to a reduced number of arriving states for the 1Se to 1Pe transition. Then, the electron cools down from $1P_e$ to $1S_e$ (end of regime I), this relaxation time $\tau_{P\rightarrow S}$ has been found to be 3.5 ps. This duration is in line with intraband relaxation dynamic in CdSe or HgTe[21–23] nanocrystals for which the relaxation decays are found to be in the 1-10 ps range[24]. Note that in the case of pristine HgTe, only a negative signal is observed (middle panel of **Figure 3**a).

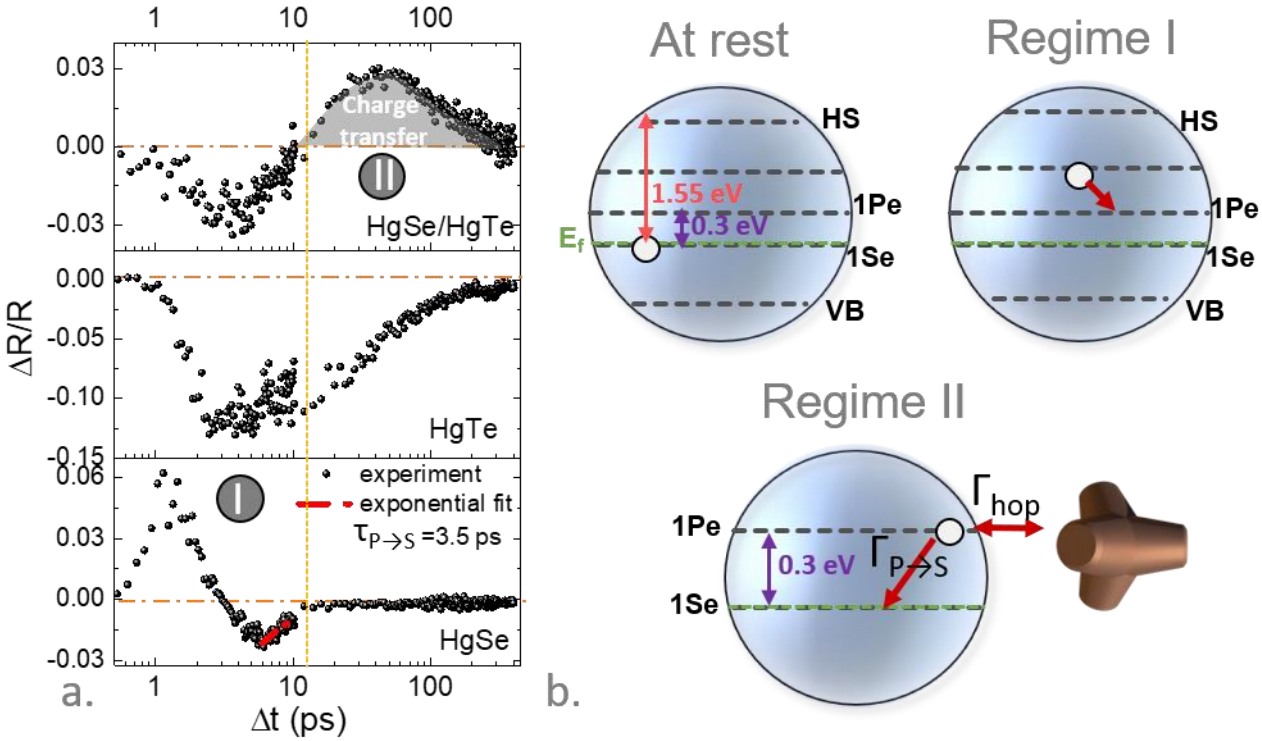

Figure 3 Carrier relaxation in array of HgX nanocrystals*. a. Transient reflectivity signal as a function of time for the film made of HgSe (bottom), HgTe (middle) and HgSe/HgTe mixture (top).*

The yellow vertical dashed line splits the regime I and II. b. Schematic of the HgSe NC electronic structure for different time ranges as defined in the bottom panel of part a.

In the case of the mixture (top panel of **Figure 3**a), the transient reflectivity signal is first negative. We then observe a positive contribution at long (>10 ps- regime II in **Figure 3**) time scale, a duration longer than intraband relaxation in both pristine materials. The observation of this signal, that is not observed in any of the two pristine materials is interpreted as the signature of the charge transfer between HgSe and HgTe. Indeed, in the mixture, there is a new relaxation pathway for carriers, where carrier can relax either within the initial particle or through charge transfer. The fact that we observe a positive signal suggests that electron transfer occurs from HgTe to HgSe. Carrier excited in HgTe ends up increasing the population of HgSe which increase the intraband absorption. This relaxation from HgTe to HgSe is consistent with the band alignment revealed by photoemission (figure S7) and also with the non-unity efficiency of the charge transfer from HgSe to HgTe revealed by the photocurrent spectrum (**Figure 2**b)

This charge transfer hypothesis is further reinforced by the fact that charge transfer characteristic time scale is found to be in the 30 – 50 ps range. A time scale that actually matches the hopping time. In a diffusive model, the latter is given by $\tau_{hop} = \frac{eR^2}{\mu k_b T}$ with *e* the proton charge, *R* the particle radius, μ the carrier mobility, k_b the Boltzmann constant and *T* the temperature. Because the transfer occurs between two types of particles, we generalized this expression to $\tau_{HgSe \rightarrow HgTe} = \frac{eR_{HgSe}R_{HgTe}}{\mu k_b T}$≈50 ps, assuming $R_{HgSe} = 2.5\,nm$, $R_{HgTe} = 5\,nm$ and $\mu \approx 10^{-2}$ cm^2.V^{-1}s^{-1}.[25,26] This value well matches the typical dynamics of the new positive contribution observed in the mixture. The determined dynamics also explain the relative magnitude of the intraband contribution in the photocurrent spectrum. For a carrier in the $1P_e$ state of HgSe, two relaxation paths are possible: a charge transfer within 30 ps or an internal relaxation in 3.5 ps. Thus, the efficiency of the charge transfer is only $\frac{\tau_{P \rightarrow S}}{\tau_{HgSe \rightarrow HgTe}}$=12% which should be considered as an order of magnitude given the temporal broadening of each feature. This is on the other hand consistent with the 17% ratio that has been determined from the photocurrent magnitude in **Figure 2**b.

While we have revealed that the fast coupling between the two materials is responsible for the enhanced detection performance, an open question is still unaddressed at this stage: the reduction of the intraband absorption resulting from the reduction of the HgSe volume fraction. Increasing the film thickness[27] might be a possible strategy. However, this approach is generally balanced by the short transport diffusion length,[28,29] meaning that thicker films, in spite of larger absorption, do not necessarily generate more photocurrent. Here we rather choose to couple the intraband absorbing layer to an optical nano-resonator. This strategy allows a multi-pass of the light through the film, leading to an absorption enhancement while maintaining the film thickness compatible with the transport diffusion length. Several types of resonators have already been coupled to NCs to enhance the absorption including Fabry-Pérot[10,30,31] cavities or plasmonic gratings. Here we choose to focus on Guided Mode Resonators (GMRs).[13,32,33] The latter relies on the diffraction of a propagative mode, while most plasmonic approaches are based on near field diffraction. As a result, the electromagnetic field is not necessarily in the immediate vicinity of the metal grating, reducing thermal losses. A schematic of the targeted device is shown in **Figure 4**a and additional information relative to the fabrication are given in figure S10-11. A gold mirror is deposited on Si/SiO_2 substrate and is used to generate a back side reflection. We then deposit, by atomic layer deposition, a thin (40 nm) layer of alumina, that isolates the bottom gold mirror from the top deposited gold grating. The latter has a dual role: to (i) generate the GMR and (ii) is used as interdigitated electrode for

transport. The period p of the grating is chosen so that $p=\lambda/n$, where λ is the resonance wavelength and n the refractive index of the film. We use electromagnetic simulations based on Rigorous Coupled-Wave Analysis[34] (RCWA) to simulate the structure and optimize other geometrical parameters (height of the electrode, thicknesses of alumina and NCs film). Simulations of the GMR absorption are given in **Figure 4**b-e and S8-9. The benefit of the GMR electrodes compared with reference interdigitated electrodes is shown in **Figure 4**b. In particular, we observe a clear absorption resonance at 4.4 µm (i.e., 2200 cm^{-1}) which is the main targeted one. The GMR signal being the result of a 1D grating, we expect the signal to be strongly polarized and the resonance occurs only along TM polarization (**Figure 4**c). Using infrared microscopy, we measure the device absorption. Optics induce a 15 ° angle for light collection responsible for a shift of the peak resulting from the device dispersion (see dispersion map in figure S9). A comparison of the experimental and simulated absorption is shown in **Figure 4**d and displays a good correlation for the energy of the resonance. Experimental peaks are broader but this is mostly the effect of optics which actually collect light with a 10 ° angle around a 15 ° tilt. In addition to the targeted resonance designed to match the intraband absorption of HgSe, we observe several additional resonances at 1.76, 1.88, 2.44, 2.84, 3.96 and 4.48 µm. A spatial mapping of the absorption loss for each resonance is given in figure S8 and **Figure 4**e. For some of them the losses are clearly located within the metal and will not contribute to the photocurrent. In table S3, we provide an estimation of the absorption occurring within the NC film for each peak. Out of these six resonances, the two main contributions expected are the one at 4.4 µm (matching the intraband contribution of HgSe) and the one at 2.44 µm (matching the interband signal of HgTe).

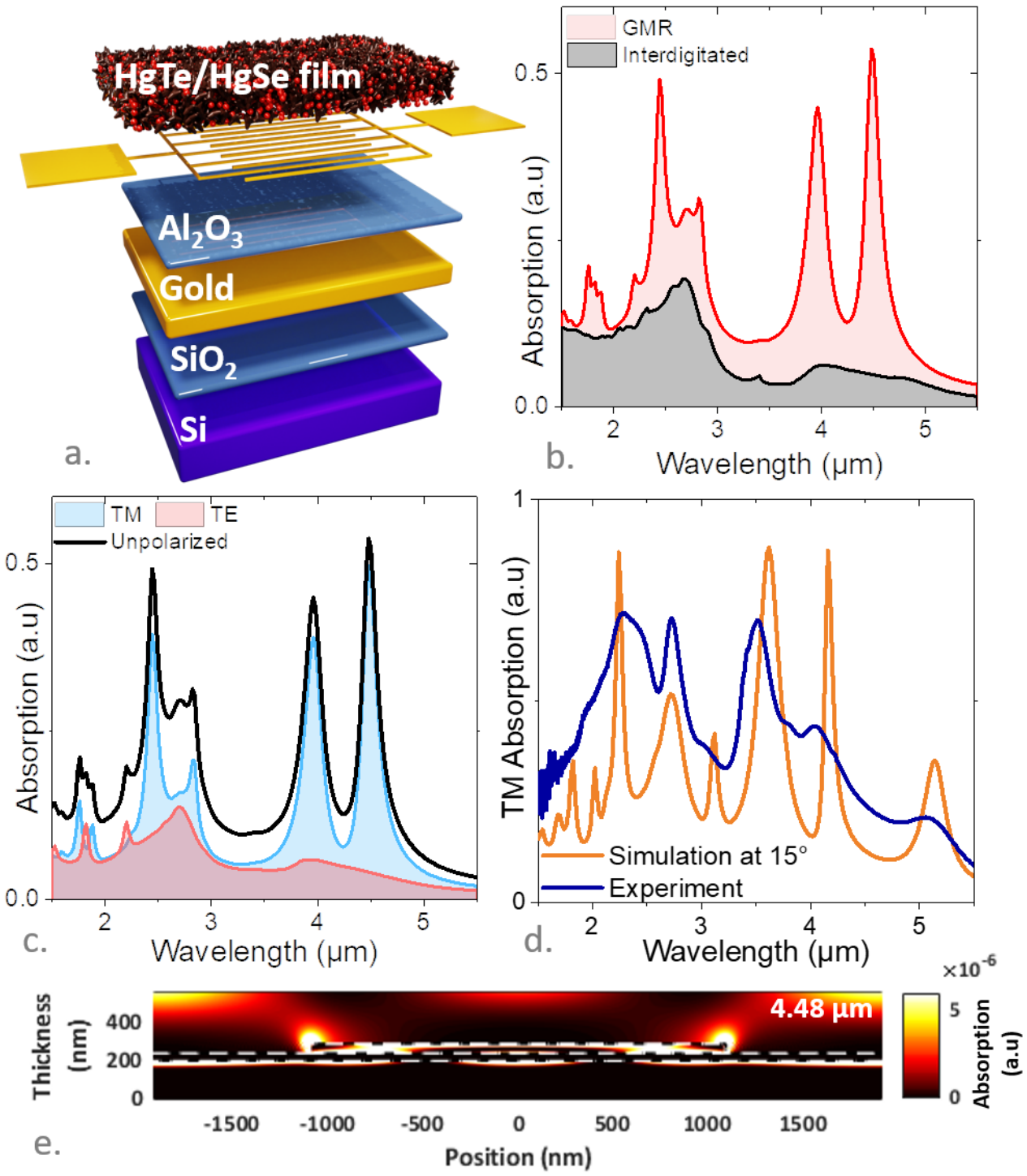

Figure 4 Intraband guided mode resonator. *a. Schematic of the GMR device coupled to an intraband absorbing film made of HgSe/HgTe NC mixture. b. Simulated absorption spectra for reference interdigitated electrodes (i.e., without resonance) and for GMR electrodes. c. Simulated absorption spectrum for GMR electrodes for unpolarized light and its TE and TM component. d. Comparion of the measured absorption (mean collect angle is 15°, with 10° aperture) and simulated absorption with a 15 ° angle (plane wave) along TM polarization. e. Absorption cross section map at 4.48 μm. The colored part correspond to absorption.*

This prediction can be confirmed by measuring the photocurrent spectra of the device along the two polarizations, see **Figure 5**a. While the TE polarization only presents the same feature as the one observed for the reference electrode, in TM we observe two highly enhanced signal matching the

interband of HgTe and the intraband of HgSe. The latter is notably enhanced by a factor 4 compared to the TE polarization. To better quantify the benefit of the GMR electrode, we then illuminate the sample with a quantum cascade laser that is spectrally matched with the intraband absorption. This way, we can exclude contribution from high energy absorbing transitions. We then plot the ratio of the photocurrent over the dark current as a function of temperature and observe a clear enhancement corresponding to a factor 4. Alternatively, the GMR enables an increase of the operating temperature by 80 K (**Figure 5**b) with respect to the device without light trapping (*i.e.,* interdigitated electrodes).

Under a blackbody illumination (filtered with a Ge window to remove signal below 2 µm), we have determined the device responsivity to be 3 $mA.W^{-1}$, with only a weak temperature dependence (**Figure 5**c). Using a pulsed QCL matching the intraband we determine the rise and fall time to be 170 and 150 ns respectively, see inset of **Figure 5**c. The noise in the device appears to be 1/f limited,[35,36] see figure S12. The specific detectivity has been determined to be 10^9 Jones at 80 K for a 5 µm cut-off wavelength (under 1.5 V and for signal at 1 kHz, see **Figure 5**d) and drops by one decade if the temperature is increased up to 160 K. A comparison of this performance with state-of-the-art nanocrystal-based intraband material is provided in table S4, and show that the device is clearly among the best performing ones.

To summarize, we have used a mixture of HgSe and HgTe as a dye sensitized infrared sensor where the infrared sensor occurs through intraband absorption. Such hybrid material preserves the intraband absorption of HgSe while reducing the dark current, increasing the activation energy and fastening the time-response. We have also unveiled the carrier dynamics in this material using infrared transient spectroscopy. We show that the relaxation of the $1P_e$ state to the $1S_e$ state in HgSe occurs within ≈ 3.5 ps. The mixture displays a new feature that is not present in pristine materials which we attribute to charge transfer. The latter process occurs with a dynamic of 30 – 60 ps that can be related to the hopping time from HgSe to HgTe. Lastly, to improve the device performance we have coupled this hybrid material to a guided mode resonator, which resonance spectrally matches the intraband absorption. The photocurrent signal resulting from the intraband contribution is enhanced by a factor 4. This enables an increase of the operating temperature by 80 K compare to the reference device without resonator. The achieved detectivity, for 5 µm cut-off detection, reaches 10^9 Jones at 80 K and presents a time-response below 200 ns matching state-of-the-art devices based on intraband absorption.

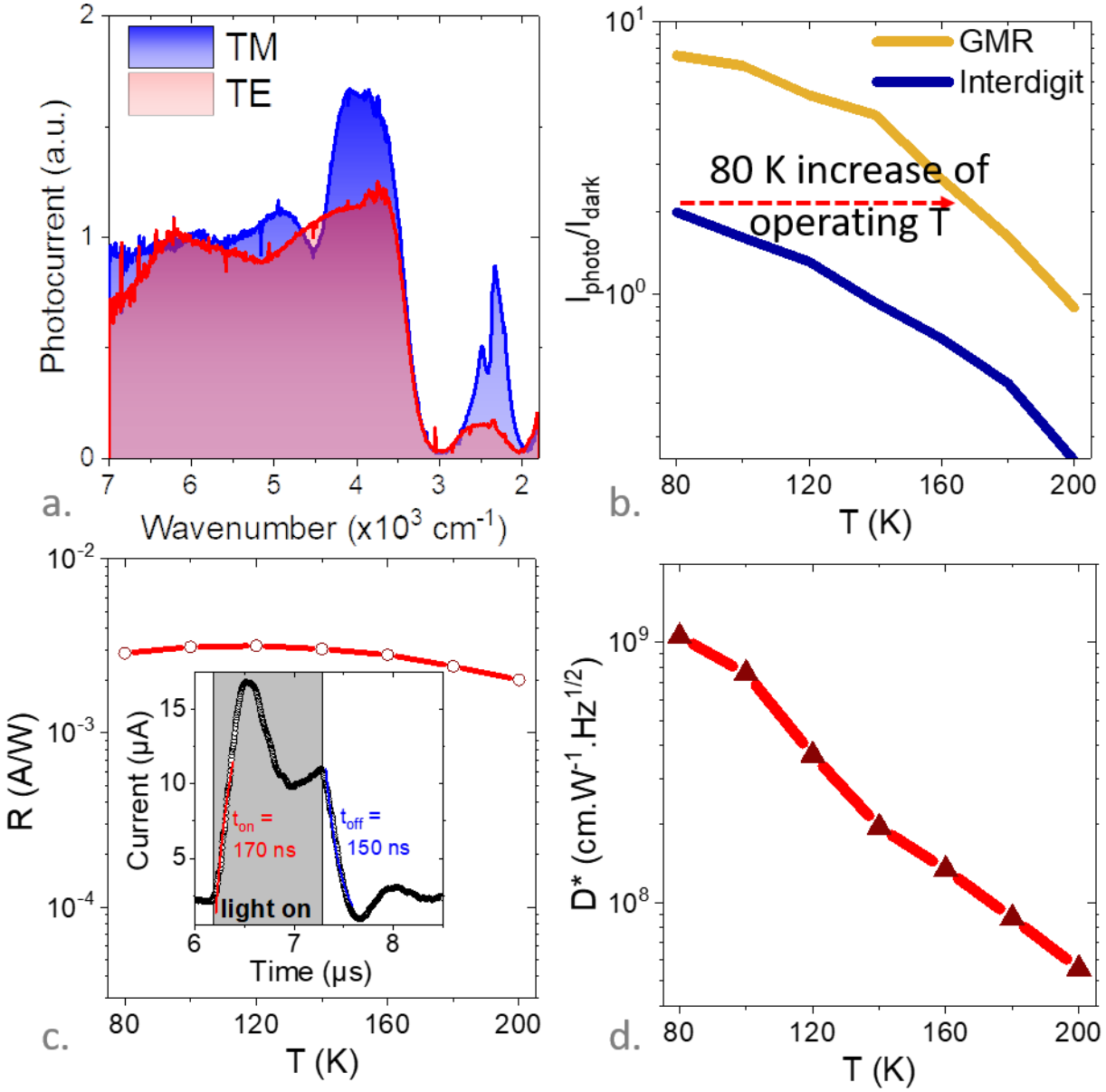

Figure 5 Performance of the intraband device coupled to GMR*. a. Photocurrent, under 0.1 V and at 80 K, spectrum for the GMR device along the two polarizations. b. Ratio of the intraband photocurrent (i.e., QCL illumination at 4.4 μm) over the dark current as a function of temperature for reference interdigitated electrodes (i.e., without resonance) and for GMR electrodes. c. Responsivity, at 1.5 V, under blackbody illumination for the GMR device as a function of temperature. The inset is the photocurrent time trace as a response to a 1 μs long pulse of light at 4.4 μm, spectrally matched with intraband absorption. d. Specific detectivity (at 1 kHz, under 1.5 V) for the GMR device as a function of temperature under blackbody illumination.*

METHODS

Chemicals: Mercury chloride ($HgCl_2$, Sigma-Aldrich, 99%), mercury acetate ($Hg(OAc)_2$, Alfa Aesar, >98%), **Mercury compounds are highly toxic. Handle them with special care.** tellurium powder (Te, Sigma-Aldrich, 99.99%), selenium powder (Se, Alfa Aesar, >99%) trioctylphosphine (TOP, Alfa, 90%), oleic acid (OA, Sigma, 90%), oleylamine (OLA, Acros, 80-90%), dodecanethiol (DDT, Sigma-Aldrich, 98%), lithium perchlorate ($LiClO_4$, Sigma-Aldrich, 98%), polyethylene glycol (PEG, $M_w = 6$ kg/mol), ethanol absolute anhydrous (VWR), methanol (VWR, >98%), acetone (VWR), isopropanol (IPA, VWR), hexane (VWR, 99%), 2-mercaptoethanol (MPOH, Merck, >99%), N,N

dimethylformamide (DMF, VWR), toluene (VWR, 99.8 %), methylisobutylketone (MIBK, VWR, >98.5%). All chemicals are used without further purification.

1 M TOP:Te precursor: 2.54 g of Te powder is mixed in 20 mL of TOP in a three neck flask. The flask is kept under vacuum at room temperature for 5 min and then the temperature is raised to 100 °C. Furthermore, degassing of flask is conducted for the next 20 min. The atmosphere is switched to nitrogen and the temperature is raised to 275 °C. The solution is stirred until a clear orange coloration is obtained. The flask is cooled down to room temperature and the color change to yellow. Finally, this solution is transferred to a nitrogen filled glove box for storage.

1 M TOP:Se precursor: 1.54 g of Se powder is sonicated in 20 mL of TOP until a colorless solution is obtained

HgSe 2.2k: In a 50 mL three neck flask, 500 mg of $Hg(OAc)_2$, 10 mL of oleic acid and 25 mL of oleylamine are degassed under vacuum at 85 °C. Meanwhile, 1.6 mL of TOP:Se (1 M) are extracted from the glove box. After the atmosphere is switched to N_2 and the temperature stabilized at 100 °C, the TOP:Se solution is quickly injected. After 3 min, 1 mL of DDT (6.6 mmol) is injected and a water bath is used to quickly decrease quickly the temperature. The content of the flask is split over 2 tubes and EtOH is added. After centrifugation, the formed pellets are redispersed in one tube with toluene. The solution is precipitated a second time using ethanol. Again, the formed pellet is redispersed in toluene. At this step the CQDs are centrifuged in pure toluene to get rid of the lamellar phase. The solid phase is discarded. The stable phase is transferred in a weighted tube and finally precipitated using methanol. The solid is dried under vacuum for 30 min (in glove box vacuum chamber). Finally, CQDs are redispersed with a 50 $mg.mL^{-1}$ concentration in toluene.

HgTe 4k: In a 100 mL three neck flask, 543 mg of $HgCl_2$ and 50 mL of oleylamine are degassed under vacuum at 110 °C. Meanwhile, 2 mL of TOP:Te (1 M) are extracted from the glove box and mixed with 8 mL of oleylamine. After the atmosphere is switched to N_2 and the temperature stabilized at 80 °C, the TOP:Te solution is quickly injected. After 3 min, 10 mL of a mixture of DDT in toluene (10% of DDT) is injected and a water bath is used to quickly decrease quickly the temperature. The content of the flask is split over 4 tubes and MeOH is added. After centrifugation, the formed pellets are redispersed in one tube with toluene. The solution is precipitated a second time using ethanol. Again, the formed pellet is redispersed in toluene. At this step the CQDs are centrifuged in pure toluene to get rid of the lamellar phase. The solid phase is discarded. The stable phase is transferred in a weighted tube and finally precipitated using methanol. The solid is dried under vacuum for 30 min (in glove box vacuum chamber). Finally, CQDs are redispersed with a 50 $mg.mL^{-1}$ concentration in toluene.

HgSe:HgTe mixture preparation: Two solutions of HgSe and HgTe are mixed in order to obtain an absorbance ratio of 1:1. A drop of the mixture is dried on the diamond cell of a Fisher IS50 Fourier transform infrared spectrometer. In ATR configuration, between 8 000 and 400 cm^{-1} we acquire a spectrum of the mixture. Transmission electron microscopy of the mixture confirms the presence of the two materials. Their very different shape makes that they can be distinguished from the regular imaging, where HgSe appears as quasi sphere and where HgTe appears as branched particles, see Figure S2. This is then further confirms using EDX (energy dispersive spectroscopy) mapping in Figure S3 and Figure S4

Transmission electron microscopy: For TEM imaging, a drop of diluted NCs solution is casted on a copper grid covered with an amorphous carbon film. The grid is degassed overnight under secondary vacuum. A JEOL 2010F is used at 200 kV for the acquisition of pictures.

(Scanning)-Transmission Electron Microscopy ((S)-TEM) Characterization. Electron microscopy characterization was performed with a FEI Talos transmission electron microscope operating at 200 kV acceleration voltage. These characterizations include bright-field High-Resolution TEM (HRTEM), STEM (probe semi-convergence angle of 10.5 mrad) and EDX chemical analysis.

FTIR spectra: FTIR spectra are acquired using a Fisher IS50 Fourier transform infrared spectrometer. To measure CQD absorption, we use the spectrometer in ATR configuration. A drop of CQD solution is dried on the diamond cell. The source is an infrared light, and the detector is a DTGS ATR. Spectra are typically acquired between 8 000 and 400 cm^{-1} with a 4 cm^{-1} resolution and averaged over 32 spectra.

Infrared ultrafast spectroscopy: Time-resolved reflectivity measurements have been performed in a standard pump-probe setup, using a commercial laser system at 1 kHz repetition rate and centered at 800 nm, with 35 fs pulse duration and 1.5 mJ energy per pulse. The laser pulse is split into two parts, with energy balance of 10%/90%. The time delay between the two pulses is controlled by a motorized micrometric step-motor. The highest energy arm is used to pump an optical parametric amplifier (OPA), which is used to generate a beam at 4 µm (≈0.3 eV) that spectrally match the intraband signal from HgSe. For the experiment presented here, we used the 800 nm pulse as pump and the OPA pulse as probe. Typical focal spot size are around 500 microns for the pump and 250 microns for the probe. Both pump and probe pulses arrive close to the normal incidence on the sample. The pump was chopped mechanically at 0.5 kHz, and the signal was detected using a photodiode connected to a lock-in amplifier.

Photocurrent spectra: The device is enclosed in a closed-cycle cryostat and cooled down to the desired temperature. The head of the cryostat is brought in the sample compartment of a Fischer iS50 FTIR spectrometer and illumination is provided by the focused Globar source through two ZnSe windows (one on the outer cryostat enclosure and one on the cold shield). The photocurrent is amplified using a Femto DLPCA−200 transimpedance amplifier, which also serves as a bias source. Output of the amplifier is sent back to the FTIR spectrometer through the ad hoc external detector adapter. All spectra are normalized to the background spectrum, acquired with a flat-response DTGS detector in the same spectral range to account for source and optical path spectra.

Activation energy: Devices are mounted on the cold finger of a closed-cycle cryostat equipped with cold shield. The samples are cooled down to 80K, and current flow is measured with a Keithley 2634b source-meter which also biased the sample. Temperature is measured with a Lakeshore 325 temperature controller using a calibrated sensor on the sample holder. Resulting $I(T)$ curves are fitted to an Arrhenius model ($I_0 = Ae^{-E_a/kT}$) between 300 K and 80 K, allowing for the extraction of the activation energy E_a.

Responsivity measurement: The source is quantum cascade laser (QCL) at 4.4 µm or a blackbody at 980 °C placed 30 cm away from the sample. The QCL spot size is 0.17 mm². The flux can be chopped from 1 Hz to 100 kHz. Current from the device is amplified using a FEMTO DLPCA-100 at 1.5 V bias and then fed into a Rohde&Schwarz RTE 1102 oscilloscope. When the blackbody is used, a germanium filter is utilized to suppress the high energy part of the blackbody spectrum. The total power calculated according to the formula: $P = A_D.\pi.cos(\beta).sin^2(\alpha).\int_{\lambda_{min}}^{\lambda_{max}} \frac{hc^2}{\lambda^5}.\frac{1}{e^{hc/\lambda kT}}d\lambda$ where α is the solid angle illuminated, β is the angle of the sample (0° corresponds to sample perpendicular

to the light illumination), A_D is the device area, h is the Planck constant, c the light velocity, k is the Boltzmann constant and T the temperature. The light is chopped from 1 Hz to 100 Hz. The photocurrent is measured using Zurich Instruments MFLI lock-in amplifier under 1.5 V of applied bias. The sample is mounted on the cold finger of a close cycle cryostat.

Noise measurement. Current from the device (at 1.5 V bias, kept in the dark) is amplified by a Femto DLPCA-200, then fed into a SRS SR780 spectrum analyzer. The sample is mounted on the cold finger of a close cycle cryostat.

Detectivity determination. The specific detectivity (in Jones) of the sample is determined using the formula: $D^* = \frac{R\sqrt{A}}{S_I}$, where R (in A.W^{-1}) is the responsivity, S_I is the noise (A/$\sqrt{Hz}$) and A the area of the device (cm²).

Supporting Information

This material is available free of charge via the internet at http://pubs.acs.org. Supporting Information include (*i*) additional material characterization (microscopy and spectroscopy) (*ii*) additional electromagnetic simulations (absorption amp and dispersion amp), (*iii*) procedure for device fabrication (*iv*) procedure for device characterization and (*v*) comparison of performance with state-of-the-art intraband devices.

COMPETING INTEREST

The authors declare no competing financial interest.

ACKNOWLEDEGMENTS

Funding sources

The project is supported by ERC starting grant blackQD (grant n° 756225) and Ne2Dem (grant n° 853049). We acknowledge the use of clean-room facilities from the “Centrale de Proximité Paris-Centre”. This work has been supported by the Region Ile-de-France in the framework of DIM Nano-K (grant dopQD). This work was supported by French state funds managed by the ANR within the Investissements d'Avenir programme under reference ANR-11-IDEX-0004-02, and more specifically within the framework of the Cluster of Excellence MATISSE and also by the grant IPER-Nano2, Copin (ANR-19-CE24-0022), Frontal (ANR-19-CE09-0017), Graskop (ANR-19-CE09-0026), NITQuantum (ANR-20-ASTR-0008-01), Bright (ANR-21-CE24-0012-02) and MixDferro (ANR-21-CE09-0029). AC thanks Agence innovation defense for PhD funding. DB acknowledges the financial support from the French department of defense (DGA) in the frame of the Oscillateur térahertz project (grant n° 2018 60 0071 00 470 75 01)

REFERENCES

(1) Faist, J.; Capasso, F.; Sivco, D. L.; Sirtori, C.; Hutchinson, A. L.; Cho, A. Y. Quantum Cascade Laser. *Science* **1994**, *264*, 553–556.

(2) Schneider, H.; Liu, H. C. *Quantum Well Infrared Photodetectors: Physics and Applications*; Springer Series in Optical Sciences; Springer-Verlag: Berlin Heidelberg, 2007.

(3) Tang, X.; Wu, G. fu; Lai, K. W. C. Plasmon Resonance Enhanced Colloidal HgSe Quantum Dot Filterless Narrowband Photodetectors for Mid-Wave Infrared. *J. Mater. Chem. C* **2017**, *5*, 362–369.
(4) Deng, Z.; Jeong, K. S.; Guyot-Sionnest, P. Colloidal Quantum Dots Intraband Photodetectors. *ACS Nano* **2014**, *8*, 11707–11714.
(5) Lhuillier, E.; Scarafagio, M.; Hease, P.; Nadal, B.; Aubin, H.; Xu, X. Z.; Lequeux, N.; Patriarche, G.; Ithurria, S.; Dubertret, B. Infrared Photodetection Based on Colloidal Quantum-Dot Films with High Mobility and Optical Absorption up to THz. *Nano Lett.* **2016**, *16*, 1282–1286.
(6) Gréboval, C.; Chu, A.; Goubet, N.; Livache, C.; Ithurria, S.; Lhuillier, E. Mercury Chalcogenide Quantum Dots: Material Perspective for Device Integration. *Chem. Rev.* **2021**, *121*, 3627–3700.
(7) Ramiro, I.; Özdemir, O.; Christodoulou, S.; Gupta, S.; Dalmases, M.; Torre, I.; Konstantatos, G. Mid- and Long-Wave Infrared Optoelectronics via Intraband Transitions in PbS Colloidal Quantum Dots. *Nano Lett.* **2020**, *20*, 1003–1008.
(8) Qu, J.; Goubet, N.; Livache, C.; Martinez, B.; Amelot, D.; Gréboval, C.; Chu, A.; Ramade, J.; Cruguel, H.; Ithurria, S.; Silly, M. G.; Lhuillier, E. Intraband Mid-Infrared Transitions in Ag2Se Nanocrystals: Potential and Limitations for Hg-Free Low-Cost Photodetection. *J. Phys. Chem. C* **2018**, *122*, 18161–18167.
(9) Hafiz, S. B.; Scimeca, M. R.; Zhao, P.; Paredes, I. J.; Sahu, A.; Ko, D.-K. Silver Selenide Colloidal Quantum Dots for Mid-Wavelength Infrared Photodetection. *ACS Appl. Nano Mater.* **2019**, *2*, 1631–1636.
(10) Tang, X.; Ackerman, M. M.; Guyot-Sionnest, P. Thermal Imaging with Plasmon Resonance Enhanced HgTe Colloidal Quantum Dot Photovoltaic Devices. *ACS Nano* **2018**, *12*, 7362–7370.
(11) Robin, A.; Livache, C.; Ithurria, S.; Lacaze, E.; Dubertret, B.; Lhuillier, E. Surface Control of Doping in Self-Doped Nanocrystals. *ACS Appl. Mater. Interfaces* **2016**, *8*, 27122–27128.
(12) Livache, C.; Martinez, B.; Goubet, N.; Gréboval, C.; Qu, J.; Chu, A.; Royer, S.; Ithurria, S.; Silly, M. G.; Dubertret, B.; Lhuillier, E. A Colloidal Quantum Dot Infrared Photodetector and Its Use for Intraband Detection. *Nat Commun* **2019**, *10*, 2125.
(13) Chu, A.; Gréboval, C.; Goubet, N.; Martinez, B.; Livache, C.; Qu, J.; Rastogi, P.; Bresciani, F. A.; Prado, Y.; Suffit, S.; Ithurria, S.; Vincent, G.; Lhuillier, E. Near Unity Absorption in Nanocrystal Based Short Wave Infrared Photodetectors Using Guided Mode Resonators. *ACS Photonics* **2019**, *6*, 2553–2561.
(14) Lhuillier, E.; Ribet-Mohamed, I.; Rosencher, E.; Patriarche, G.; Buffaz, A.; Berger, V.; Carras, M. Interface Roughness Transport in Terahertz Quantum Cascade Detectors. *Appl. Phys. Lett.* **2010**, *96*, 061111.
(15) Kim, J.; Choi, D.; Jeong, K. S. Self-Doped Colloidal Semiconductor Nanocrystals with Intraband Transitions in Steady State. *Chem. Commun.* **2018**, *54*, 8435–8445.
(16) Qu, J.; Livache, C.; Martinez, B.; Gréboval, C.; Chu, A.; Meriggio, E.; Ramade, J.; Cruguel, H.; Xu, X. Z.; Proust, A.; Volatron, F.; Cabailh, G.; Goubet, N.; Lhuillier, E. Transport in ITO Nanocrystals with Short- to Long-Wave Infrared Absorption for Heavy-Metal-Free Infrared Photodetection. *ACS Appl. Nano Mater.* **2019**, *2*, 1621–1630.
(17) Martinez, B.; Livache, C.; Notemgnou Mouafo, L. D.; Goubet, N.; Keuleyan, S.; Cruguel, H.; Ithurria, S.; Aubin, H.; Ouerghi, A.; Doudin, B.; Lacaze, E.; Dubertret, B.; Silly, M. G.; Lobo, R. P. S. M.; Dayen, J.-F.; Lhuillier, E. HgSe Self-Doped Nanocrystals as a Platform to Investigate the Effects of Vanishing Confinement. *ACS Appl. Mater. Interfaces* **2017**, *9*, 36173–36180.
(18) Chee, S.-S.; Gréboval, C.; Magalhaes, D. V.; Ramade, J.; Chu, A.; Qu, J.; Rastogi, P.; Khalili, A.; Dang, T. H.; Dabard, C.; Prado, Y.; Patriarche, G.; Chaste, J.; Rosticher, M.; Bals, S.; Delerue, C.; Lhuillier, E. Correlating Structure and Detection Properties in HgTe Nanocrystal Films. *Nano Lett.* **2021**, *21*, 4145–4151.
(19) Moghaddam, N.; Gréboval, C.; Qu, J.; Chu, A.; Rastogi, P.; Livache, C.; Khalili, A.; Xu, X. Z.; Baptiste, B.; Klotz, S.; Fishman, G.; Capitani, F.; Ithurria, S.; Sauvage, S.; Lhuillier, E. The

Strong Confinement Regime in HgTe Two-Dimensional Nanoplatelets. *J. Phys. Chem. C* **2020**, *124*, 23460–23468.
(20) Livache, C.; Goubet, N.; Gréboval, C.; Martinez, B.; Ramade, J.; Qu, J.; Triboulin, A.; Cruguel, H.; Baptiste, B.; Klotz, S.; Fishman, G.; Sauvage, S.; Capitani, F.; Lhuillier, E. Effect of Pressure on Interband and Intraband Transition of Mercury Chalcogenide Quantum Dots. *J. Phys. Chem. C* **2019**, *123*, 13122–13130.
(21) Ruppert, M.; Bui, H.; Sagar, L. K.; Geiregat, P.; Hens, Z.; Bester, G.; Huse, N. Intraband Dynamics of Mid-Infrared HgTe Quantum Dots. *Nanoscale* **2022,** asap.https://doi.org/10.1039/D1NR07007J
(22) Apretna, T.; Massabeau, S.; Gréboval, C.; Goubet, N.; Tignon, J.; Dhillon, S.; Carosella, F.; Ferreira, R.; Lhuillier, E.; Mangeney, J. Few Picosecond Dynamics of Intraband Transitions in THz HgTe Nanocrystals. *Nanophotonics* **2021**, *10*, 2753–2763.
(23) Qu, J.; Weis, M.; Izquierdo, E.; Mizrahi, S. G.; Chu, A.; Dabard, C.; Gréboval, C.; Bossavit, E.; Prado, Y.; Péronne, E.; Ithurria, S.; Patriarche, G.; Silly, M. G.; Vincent, G.; Boschetto, D.; Lhuillier, E. Electroluminescence from Nanocrystals above 2 µm. *Nat. Photon.* **2022**, *16*, 38–44.
(24) Guyot-Sionnest, P.; Shim, M.; Matranga, C.; Hines, M. Intraband Relaxation in CdSe Quantum Dots. *Phys. Rev. B* **1999**, *60*, R2181–R2184.
(25) Martinez, B.; Ramade, J.; Livache, C.; Goubet, N.; Chu, A.; Gréboval, C.; Qu, J.; Watkins, W. L.; Becerra, L.; Dandeu, E.; Fave, J. L.; Méthivier, C.; Lacaze, E.; Lhuillier, E. HgTe Nanocrystal Inks for Extended Short-Wave Infrared Detection. *Advanced Optical Materials* **2019**, *7*, 1900348.
(26) Gréboval, C.; Noumbe, U.; Goubet, N.; Livache, C.; Ramade, J.; Qu, J.; Chu, A.; Martinez, B.; Prado, Y.; Ithurria, S.; Ouerghi, A.; Aubin, H.; Dayen, J.-F.; Lhuillier, E. Field-Effect Transistor and Photo-Transistor of Narrow-Band-Gap Nanocrystal Arrays Using Ionic Glasses. *Nano Lett.* **2019**, *19*, 3981–3986.
(27) Fan, J. Z.; Vafaie, M.; Bertens, K.; Sytnyk, M.; Pina, J. M.; Sagar, L. K.; Ouellette, O.; Proppe, A. H.; Rasouli, A. S.; Gao, Y.; Baek, S.-W.; Chen, B.; Laquai, F.; Hoogland, S.; Arquer, F. P. G. de; Heiss, W.; Sargent, E. H. Micron Thick Colloidal Quantum Dot Solids. *Nano Lett.* **2020**, *20*, 5284–5291.
(28) Chu, A.; Gréboval, C.; Prado, Y.; Majjad, H.; Delerue, C.; Dayen, J.-F.; Vincent, G.; Lhuillier, E. Infrared Photoconduction at the Diffusion Length Limit in HgTe Nanocrystal Arrays. *Nat Commun* **2021**, *12*, 1794.
(29) Lan, X.; Chen, M.; Hudson, M. H.; Kamysbayev, V.; Wang, Y.; Guyot-Sionnest, P.; Talapin, D. V. Quantum Dot Solids Showing State-Resolved Band-like Transport. *Nat. Mater.* **2020**, *19*, 323–329.
(30) Tang, X.; Ackerman, M. M.; Shen, G.; Guyot-Sionnest, P. Towards Infrared Electronic Eyes: Flexible Colloidal Quantum Dot Photovoltaic Detectors Enhanced by Resonant Cavity. *Small* **2019**, *15*, 1804920.
(31) Tang, X.; Ackerman, M. M.; Guyot-Sionnest, P. Acquisition of Hyperspectral Data with Colloidal Quantum Dots. *Laser & Photonics Reviews* **2019**, *13*, 1900165.
(32) Rastogi, P.; Chu, A.; Gréboval, C.; Qu, J.; Noumbé, U. N.; Chee, S.-S.; Goyal, M.; Khalili, A.; Xu, X. Z.; Cruguel, H.; Ithurria, S.; Gallas, B.; Dayen, J.-F.; Dudy, L.; Silly, M. G.; Patriarche, G.; Degiron, A.; Vincent, G.; Lhuillier, E. Pushing Absorption of Perovskite Nanocrystals into the Infrared. *Nano Lett.* **2020**, *20*, 3999–4006.
(33) Gréboval, C.; Chu, A.; Magalhaes, D. V.; Ramade, J.; Qu, J.; Rastogi, P.; Khalili, A.; Chee, S.-S.; Aubin, H.; Vincent, G.; Bals, S.; Delerue, C.; Lhuillier, E. Ferroelectric Gating of Narrow Band-Gap Nanocrystal Arrays with Enhanced Light–Matter Coupling. *ACS Photonics* **2021**, *8*, 259–268.
(34) Hugonin, J. P.; Lalanne, P. RETICOLO Software for Grating Analysis. **2021**-01-04, arXiv:2101.00901 [physics]. (accessed 2022-01-10).
(35) Liu, H.; Lhuillier, E.; Guyot-Sionnest, P. 1/f Noise in Semiconductor and Metal Nanocrystal Solids. *Journal of Applied Physics* **2014**, *115*, 154309.

(36) Lai, Y.; Li, H.; Kim, D. K.; Diroll, B. T.; Murray, C. B.; Kagan, C. R. Low-Frequency (1/f) Noise in Nanocrystal Field-Effect Transistors. *ACS Nano* **2014**, *8*, 9664–9672.

TOC graphic

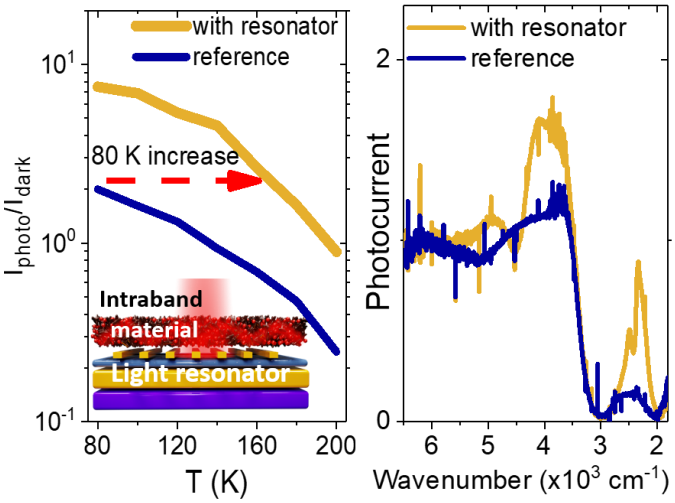
with resonator
reference
80 K increase
Intraband
material
Light resonator
I_{photo}/I_{dark}
T (K)
Photocurrent
Wavenumber (x10^3 cm^{-1})